Geophysical Journal International

Geophys. J. Int. (2010) **182,** 97–112 doi: 10.1111/j.1365-246X.2010.04629.x

Lithospheric flexure modelling seaward of the Chile trench: implications for oceanic plate weakening in the Trench Outer Rise region

Eduardo Contreras-Reyes[1] and Axel Osses[2,3]

[1] *Departamento de Geofísica, Facultad de Ciencias de Físicas y Matemáticas, Universidad de Chile, Santiago, Chile. E-mail: econtreras@dgf.uchile.cl*
[2] *Departamento de Ingeniería Matemática, Facultad de Ciencias de Físicas y Matemáticas, Universidad de Chile, Santiago, Chile*
[3] *Centro de Modelamiento Matemático (UMI 2807 CNRS), Chile*

Accepted 2010 April 14. Received 2010 March 27; in original form 2009 December 17

SUMMARY

The Chilean subduction zone presents a unique opportunity to study trench outer rise deformation of the subducting oceanic lithosphere at different thermal ages. The shape of the outer rise for plate ages ranging from 0 to 50 Ma is predicted by using an elastic plate model with variable elastic thickness $T_e(x)$ as a function of the distance measured from the trench axis. In addition, the uncertainties of our results are estimated by performing a Monte Carlo-type analysis and we considered explicitly the sediment loading effect on the lithospheric flexure in regions where the trench is heavily sedimented.

The results show a systematic reduction in T_e of up to 50 per cent (or reduction in the flexural rigidity D of up to ~90 per cent) from the peak of the outer rise to the trench axis. The reduction in T_e and D observed in most of the bathymetric profiles is coincident with (i) high plate curvatures ($>5 \times 10^{-7}$ m^{-1}), (ii) strong bending moments ($>10^{16}$ N m), (iii) pervasive fracturing and faulting of the oceanic basement (as imaged by high-resolution bathymetry data) and (iv) reduction in crustal and mantle seismic velocities. The reduction in flexural rigidity towards the trench suggests a weakening of the oceanic lithosphere and is interpreted to be caused partially by fracturing and a likely increase in fluid-pore pressure. In general, our estimates do not show consistent increases in elastic thickness as a function of plate age. This result suggests that either T_e is independent of plate age or T_e depends strongly on other factors. These factors could include lithospheric weakening due to hydro-fracturing and the loading history of the plate prior to subduction.

Key words: Elasticity and anelasticity; Subduction zone processes; Dynamics of lithosphere and mantle; Lithospheric flexure; Fractures and faults.

1 INTRODUCTION

Bending of oceanic plates prior to subduction is largely due to the negative buoyancy of the sinking plate (slab pull). Because the cold slowly deforming interior of the plate is stiff and behaves elastically, the plate is able to transmit stresses for several thousand kilometres (e.g. Capitanio *et al.* 2009). A consequence of the plate bending is the formation of a prominent fore-bulge (the outer-rise) prior to subduction of the oceanic plate. The wavelength and amplitude of the outer rise depends on the rheology and stress state of the oceanic plate. The shape of the outer rise has been modelled using a mechanically strong lithosphere, loaded on the arcward side of the trench axis, overlying a weak astenosphere. Hanks (1971), Watts & Talwani (1974), Parsons & Molnar (1976), Harris & Chapman 1994, Levitt & Sandwell (1995) and Bry & White (2007) have successfully modelled the flexure of the lithosphere prior to subduction using an elastic rheology with constant flexural rigidity $D = \frac{E T_e^3}{12(1-\nu^2)}$, which is a measure of the resistance of the lithosphere to flexure in response to loading. The Young's modulus, E, and Poisson's ratio, ν, are material properties commonly treated as constant. With this assumption, D depends entirely on the elastic thickness T_e. It has been determined, however, that the elastic model with uniform T_e or D cannot adequately replicate near-trench bathymetry for steeply dipping sea-floor characterized by extremely high curvatures (Turcotte *et al.* 1978; Judge & McNutt 1991).

Sharp bending and inelastic behaviour of the flexed lithosphere occur when bending stresses exceed the yield strength of the lithosphere. This process results in brittle fracture of the upper part of the lithosphere and ductile flow of the lower lithosphere so that the estimated elastic thickness is much less than the true mechanical thickness (Ranalli 1994). Turcotte *et al.* (1978), for instance, used an elastic-perfectly plastic model to explain the steep slope of the lithosphere within the trench. They found that the oceanic lithosphere behaves elastically seaward of the outer rise, but towards the trench the lithosphere deviates from elastic behaviour and an elastic-perfectly plastic model more adequately explains the increase in curvature ratio when stresses exceed the yield strength of the rock. Alternatively, Judge & McNutt (1991) used an elastic rheology with variable flexural rigidity to successfully model the high curvatures when they greatly reduced the flexural rigidity towards the trench. Thus, strong bending near the trench tended to make the lithosphere substantially weaker and thinner. More realistic rheologies such as multilayer fragile–elastic–ductile have incorporated the effects of inelastic yielding using a yield strength envelope allowing any T_e measurement to be converted to the true mechanical thickness T_m (i.e. T_e at zero curvature) (Goetze & Evans 1979; McAdoo *et al.* 1978; Bodine & Watts 1979; Bodine *et al.* 1981; McAdoo *et al.* 1982; McNutt & Menard 1982; McNutt 1984). Following the method of McNutt & Menard (1982) T_m can be estimated based on T_e and curvature given the yield strength envelope which unfortunately depends upon extrapolation of laboratory data by more than 10 orders of magnitude.

Deviation from elastic behaviour of the oceanic lithosphere has been attributed to faulting in the outer rise region. For example, observations of seafloor bathymetry and seismic reflection data at several subduction zones reveal that subducting plates suffer significant crustal-scale faulting while entering the trench (Masson 1991; Ranero *et al.* 2005) as well as large tensional earthquakes (Christensen & Ruff 1983; Ranero *et al.* 2005). These processes indicate that the subducting plate undergoes permanent lithosphere-scale deformation, hydration and weakening prior to subduction. Judge & McNutt (1991) and Billen & Gurnis (2005) argued that inelastic lithospheric deformation of the subducting plate occurs from the outer rise trenchward, which results in the reduction in plate strength or flexural rigidity from the peak of the outer rise towards the trench axis as plate bending becomes stronger. Judge & McNutt (1991) studied trench-outer rise deformation off northern Chile where the oceanic plate age is 45 Ma and they found that T_e was reduced by 50 per cent while off of Peru on the younger oceanic plate (30 Ma) the elastic plate thickness was reduced only by 20 per cent. Billen & Gurnis (2005), on the other hand, studied the plate strength within the Kermadec Trench by using a viscous model and they found a clear reduction in flexural rigidity by 3–5 orders of magnitude (decrease in T_e of more than 15 km). This reduction in T_e suggests that the plate has little or no elastic strength within the trench (Billen & Gurnis 2005). Despite these strategies to explicity or implicity include inelastic deformation in flexural models, the magnitude of the reduction in the effective elastic thickness is still uncertain and nearly nothing is known about the relationship between reduced T_e and thermal age of the plate.

One appropriate place to study the elastic properties of the oceanic lithosphere at different thermal ages is the Chile subduction zone. Here the age of the oceanic Nazca Plate where it enters the trench is 0 Ma at 46°S and 50 Ma at 18°S. In this region, swath bathymetry data have imaged dense sets of bending-related faults parallel to the trench axis indicating the brittle behaviour of the upper part of the lithosphere (Grevemeyer *et al.* 2005; Ranero *et al.* 2005; Contreras-Reyes *et al.* 2007, 2008a). Recently published seismic refraction profiles have shown a systematic decrease in crustal and mantle seismic velocities in the outer-rise region which have been interpreted in terms of extensional bending-related fracturing and hydration of the oceanic lithosphere (Contreras-Reyes *et al.* 2007, 2008a; Ivandic *et al.* 2010). The region of low crustal and mantle velocities and fractured topography of the seafloor is confined in the outer rise area where bending stresses exceed the yield strength of the lithosphere resulting in deep penetrating bend faults (Ranero *et al.* 2005; Grevemeyer *et al.* 2005; Tilmann *et al.* 2008). Thus, the permeability and porosity structure of the oceanic lithosphere is expected to be strongly altered and characterized by pathways for percolation of seawater and serpentinization of the oceanic mantle (Ranero *et al.* 2005). The continuous increase in fracturing and fluid pore pressure may result in a weakening of the plate and thus a reduction in its elastic capacity.

The main aim of this study is to investigate variations in elastic thicknesses within the incoming-oceanic lithosphere caused by the increase in bending moments near the trench off Chile at different thermal ages. Our focus is to explore the existence of plate weakening at the outer rise related to bending-related faulting and its relationship with thermal age. We study the long wavelength outer rise topography of the incoming oceanic Nazca Plate along the Chile trench using bathymetry and published seismic reflection profiles perpendicular to the trench axis. We used the classical elastic plate model to keep the data analysis relative simple. However, our analysis is different from previous studies for the following reasons: (1) we present an alternative strategy of equation solution by finite differences and a semi-inversion technique of T_e, (2) we used a variable flexural rigidity $D = D(x)$ to simulate the yielding associated with the decreased strength of the lithosphere near the trench, (3) in regions where the trench is heavily sedimented we predict the top of the oceanic basement using seismic data and include the effect of sedimentary loading, and (4) we calculate the uncertainties of our T_e estimates by using the Monte Carlo method. Finally, we interpret the results in terms of inelastic processes and thermal age of the oceanic plate.

2 GEODYNAMIC SETTING

The oceanic Nazca Plate currently subducts beneath South America at a rate of ∼6.6 cm yr^{-1} (Angermann *et al.* 1999), but probably moved at mean rate of ∼8.5 cm yr^{-1} during the past several million years (DeMets *et al.* 1990). The Nazca Plate was formed in the north of the Juan Fernández Ridge (JFR) at the Pacific-Nazca spreading centre (East Pacific Rise) more than 35 Myr ago (Tebbens *et al.* 1997), whereas south of the JFR it was created at the Nazca-Antarctic spreading centre within the past 35 Ma (Herron *et al.* 1981) (Fig. 1). The age of the oceanic Nazca Plate (Tebbens *et al.* 1997; Mueller *et al.* 1997) along the Peru-Chile trench increases from 0 Ma at the Chile Triple Junction (CTJ) to a maximum of 50 Ma around 20°S (Fig. 1). North of this latitude, the continental margin changes its orientation from NNE to NW, a feature known as the Arica bend. Further to the north, the plate age decreases along the trench up to ∼28 Ma at 5°S (Fig. 1). Fracture zones cut the Chile Rise (the southern part of the Nazca-Antarctic spreading centre) into several segments (Fig. 1), resulting in abrupt changes in thermal state along the plate boundary. These segments bounded by these FZs are roughly parallel to the trench strike (Fig. 1).

The southern central Chile trench between 34°S and 45.5°S is heavily sedimented as the result of sediments delivered by the rivers and rapid glaciation denudation of the Andes (Thornburg *et al.* 1990; Bangs & Cande 1997; Voelker *et al.* 2006). Within the trench, turbidites migrate to the north as the seafloor depth becomes deeper with the plate age (Fig. 1). Fig. 1(b) shows the depths of the seafloor and top of the oceanic basement at the Chile trench axis between 20°S and 48°S. The seafloor is only 3 km deep in the vicinity of the incoming Chile Rise, where the plate age is 0 Ma. As the oceanic plate becomes older to the north, the seafloor depth increases rapidly

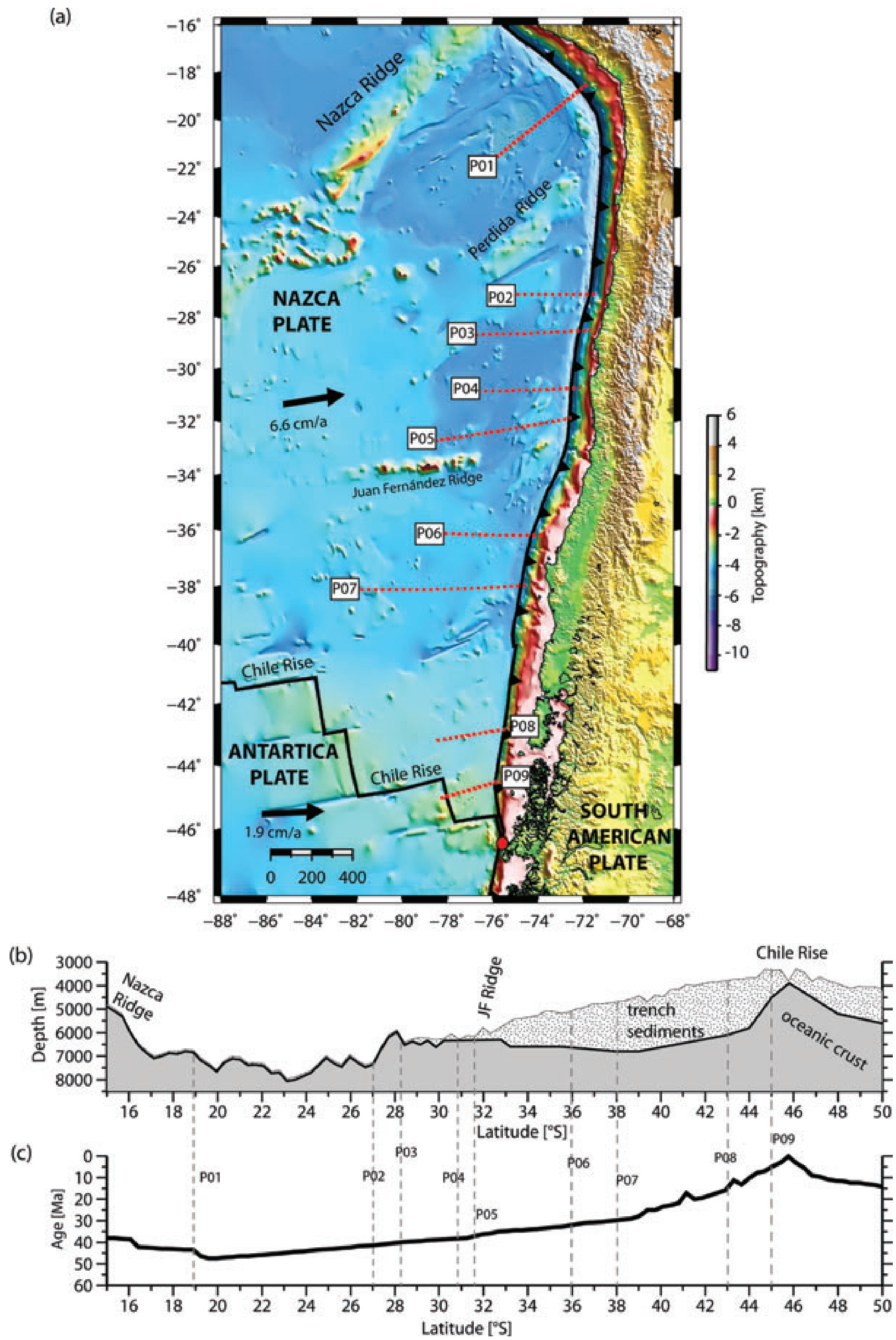

Figure 1. (a) Geodynamic setting of Nazca, Antarctic and South American plates. These plates meet at the Chile Triple Junction (CTJ), where the Chile Rise is currently subducting at ∼46.4°S. The oceanic Nazca Plate is segmented by several fracture zones, resulting in a strong variability of the age of the subducting plate. Dotted red lines are the bathymetric profiles used for flexural modelling. Bathymetric map based on GEBCO bathymetric data (Sandwell & Smith 1997). (b) Depth of the trench axis along the Chilean trench. The seafloor depth was taken from the global bathymetric grid of Sandwell & Smith (1985). Trench fill thicknesses were computed by a linear interpolation of trench-fill thickness published in seismic lines (Kopp *et al.* 2004; Flueh & Grevemeyer 2005; Contreras-Reyes *et al.* 2007; 2008a; Scherwath *et al.* 2009; Bourgois *et al.* 2000). (c) Plate age of the oceanic Nazca and Antarctic plates at the trench axis. The age of the oceanic lithosphere were taken from the global grid of Mueller *et al.* (1997).

reaching ∼5.8 km at 33°S (Fig. 1). The trench fill thickness between 34°S and ∼45°S ranges between 1.5 and 2.5 km, while north of the JFR sedimentary thickness is only about 500 m (von Huene *et al.* 1997). Further northward, the trench deepens progressively to 8 km off Antofagasta at ∼22°S and has little sediment fill (Fig. 1). The JFR behaves like a barrier for trench turbidites transport separating a sediment-starved trench axis to the north from a sediment-flooded axis to the south (von Huene *et al.* 1997). The shallow and

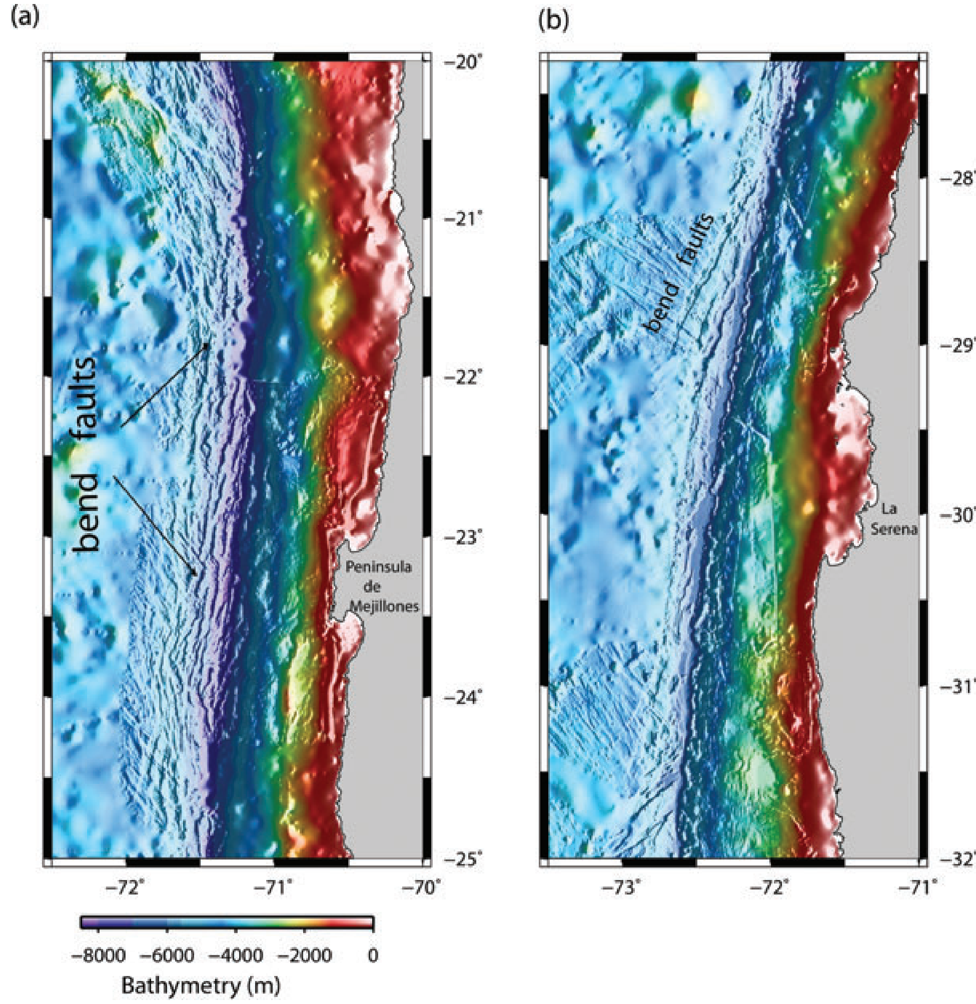

Figure 2. High-resolution bathymetric image of the seafloor off (a) north Chile (Ranero & Sallares 2004), (b) north-central Chile (Clouard, 2002, private communication) and (c) south-central Chile (Scherwath *et al.* 2006). In every region, bathymetric mapping shows the SE-NW trending topographic pattern of the tectonic fabric formed at the spreading centre, which is overprinted by bend faults. The rough basement topography is evident for every region except south of Juan Fernández Ridge (33°S) where the thick sediments cover the basement topography.

buoyant Chile Rise 'displaces' sediments to the north, thus confining between these two main oceanic features a thick sedimentary cover along the southern central Chile trench (Fig. 1).

North of the Valdivia FZ, the seafloor spreading fabric of the incoming plate strikes approximately 45° obliquely to the trench axis. In the outer rise area the seafloor fabric generated at the spreading centre and cross-cutting normal faults caused by plate bending are well imaged in multibeam bathymetric data (Fig. 2); whereas bend-faults strike approximately parallel to the trench axis and form a new fabric (Ranero *et al.* 2005). Multichannel seismic reflection data suggest that the smooth trench area mapped in the bathymetric data is caused by sediment filling the trench south of the JFR (Voelker *et al.* 2006). Under the trench fill, multichannel data reveal bending-related faults cutting across the crust–mantle boundary into the upper mantle (Diaz-Naveas 1999; Grevemeyer *et al.* 2005). Reduced crustal and mantle velocities have been imaged off Chile using seismic wide-angle data off Antofagasta (22°S) (Ranero & Sallares 2004), off Valparaíso (33°S) (Kopp *et al.* 2004), off Concepción (38°S) (Contreras-Reyes *et al.* 2008a) and off Isla de Chiloé (43°S) (Contreras-Reyes *et al.* 2007), and have been interpreted as fracturing and hydration of the upper part of the brittle oceanic lithosphere.

3 ANALYSIS STRATEGY

3.1 Data compilation

To study the flexure of the plate seaward of the Chilean trench, we extracted bathymetric profiles perpendicular to the trench axis from global data sets of bathymetry (Sandwell & Smith 1997) and high-resolution swath-mapping bathymetry where available (von Huene *et al.* 1997; Flueh *et al.* 2002; Flueh & Grevemeyer 2005). The extracted bathymetric profiles are plotted and labelled in Fig. 1 from oldest to youngest oceanic lithosphere. Profiles 01–05 cross a sediment-starved trench whereas profiles 06–09 cross a thick trench basin with up to 2.5 km of sediments (Voelker *et al.* 2006). Profiles 06–09 were chosen to be coincident with the locations of seismic profiles as follows: P06 (Flueh & Grevemeyer 2005), P07 (Contreras-Reyes *et al.* 2008a), P08 (Contreras-Reyes *et al.* 2007) and P09 (Scherwath *et al.* 2009). The idea is to model the top of the oceanic basement instead of the seafloor topography to take into account the effect of sediment loading (see Section 3.3 for further discussion). In general, we avoid extracting profiles near high oceanic features, like seamounts, that are unrelated to plate flexure (Fig. 1). To correct data for non-normality, distance values

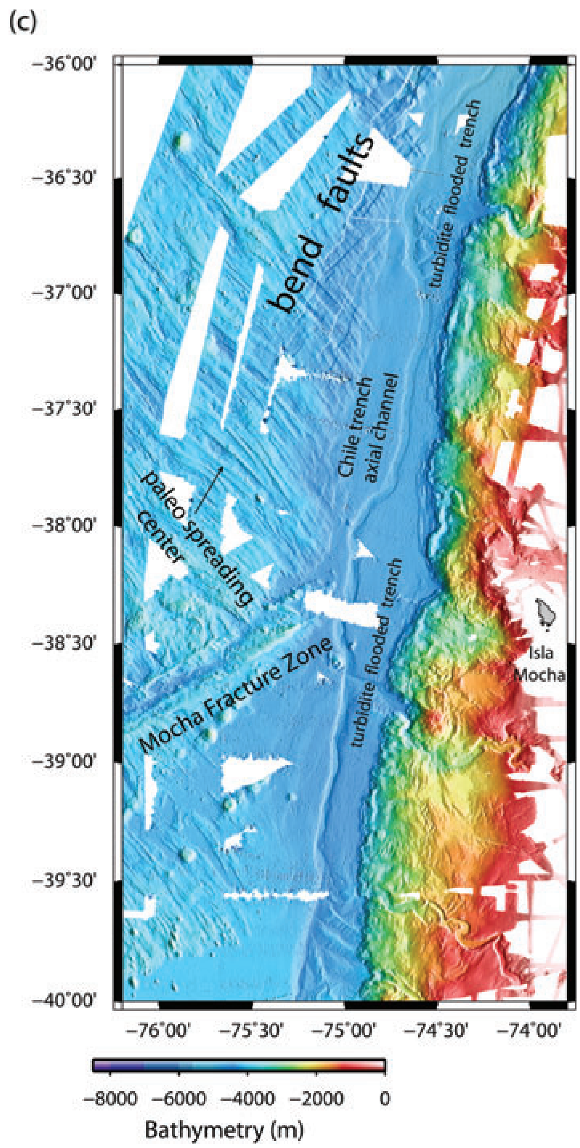

Figure 2. (*Continued.*)

were multiplied by $\cos\theta$, the angle between the profile and trench-perpendicular azimuths.

We extracted the plate age along each profile from the global age grid of Mueller *et al.* (1997) to correct the increase in seafloor depth with age by computing the depth anomaly, which is the difference between the observed bathymetry, and a theoretical depth given by the age subsidence model of Parsons & Sclater (1977). Each point was corrected as follows:

$$d(t) = 2500 + 350\sqrt{t}\ [\mathrm{m}] \qquad \text{if } t < 20 \text{ Ma and}$$

$$d(t) = 6400 - 3200e^{-t/62.8}\ [\mathrm{m}] \qquad \text{if } t \geq 20 \text{ Ma}$$

The extracted profiles are shown in Sections 3.4 and 4. Short-wavelength features that are evident in high-resolution bathymetry (Fig. 2) are related to faults that formed in the outer rise region due to plate bending. Despite the presence of irregular bathymetry that masks the elastic behaviour of the plate, the bathymetry data indicate a clear long wavelength signature (outer bulge). The southernmost profiles P06–P09 are situated where the trench is heavily sedimented. This broad sediment cover obscures most obvious features of lithospheric flexure. Therefore, we model the basement reflector taken from seismic reflection data instead of the bathymetric data. Profiles P06–P09 are characterized by a high lithospheric deflection at the trench axis and an outer rise lacking any topographic expression. The shape of these profiles is influenced, at least in part, by the heavy sediment loading.

3.2 Flexural modelling

The flexure of the oceanic lithosphere at trenches has been modelled by many authors as an elastic plate acted upon by a hydrostatic restoring force $g(\rho_m - \rho_w)w$, where w is the plate flexure, g is average gravity and ρ_m and ρ_w are mantle and water density, respectively (Fig. 3) (e.g. Caldwell *et al.* 1976; Turcotte & Schubert 1982; Levitt & Sandwell 1995; Bry & White 2007). If the applied load comprises of a horizontal force F and a bending moment M the deflection w of the plate is governed by the following ordinary differential equation:

$$-\frac{\mathrm{d}^2 M}{\mathrm{d}x^2} + \frac{\mathrm{d}}{\mathrm{d}x}\left(F\frac{\mathrm{d}w}{\mathrm{d}x}\right) + (\rho_m - \rho_w)wg = q(x), \tag{1}$$

where $q(x)$ is the load acting on the plate and the bending moment and shear force V are related to the negative curvature of the plate $\kappa = -\frac{\mathrm{d}^2 w}{\mathrm{d}x^2}$ by the flexural rigidity D by

$$M = -D\frac{\mathrm{d}^2 w}{\mathrm{d}x^2} \tag{2}$$

and

$$V = \frac{\mathrm{d}M}{\mathrm{d}x} - F\frac{\mathrm{d}w}{\mathrm{d}x}. \tag{3}$$

The boundary conditions are as follows:

(i) $w \to 0$ as $x \to +\infty$ (no flexure away from the load);
(ii) $\frac{\mathrm{d}w}{\mathrm{d}x} \to 0$ as $x \to +\infty$ (first order stability condition);
(iii) $M|_{x=0} = -M_o = -D\frac{\mathrm{d}^2 w}{\mathrm{d}x^2}|_{x=0}$ (bending moment—M_o applied at x=0);
(iv) $V|_{x=0} = -V_o = \frac{\mathrm{d}M}{\mathrm{d}x}|_{x=0}$ (shear force—V_o applied at x=0).

Unfortunately, V_o and M_o cannot be independently measured. According to Bry & White (2007) we also believe that it is very important not to fix these unknown parameters in advance (contra Jordan & Watts 2005, who calculated the size and shape of the load from topography alone and then invert for T_e and the position of the plate break). Instead, V_o and M_o are permitted to vary and we find that there are significant trade-offs between V_o, M_o and, T_e which both moderate the shape of the misfit function and affect the location of its global minimum. In this way, the vexed matter of surficial and subsurficial load characterization is sidestepped (Section 3.4).

Caldwell *et al.* (1976) conclude that even a large horizontal load F will not have a strong effect on the deformation of the plate, and F cannot be determined from bathymetric profiles with any precision. Tectonics regimes landward of subduction zones do not show evidence for large compressive stress ($\geq$500 MPa) (Molnar & Atwater 1978) and in many cases are sites of extension and spreading. Therefore, we do not include the horizontal force as a parameter in our flexural modelling (i.e. F is set to zero).

In the case of constant flexural rigidity with $q = 0$ and $F = 0$, there is an analytical solution of (1) given by (e.g. Turcotte & Schubert 1982)

$$w(x) = \frac{\alpha^2 e^{-x/\alpha}}{2D}\left[-M_o\sin\left(\frac{x}{\alpha}\right) + (V_o\alpha + M_o)\cos\left(\frac{x}{\alpha}\right)\right] \tag{4}$$

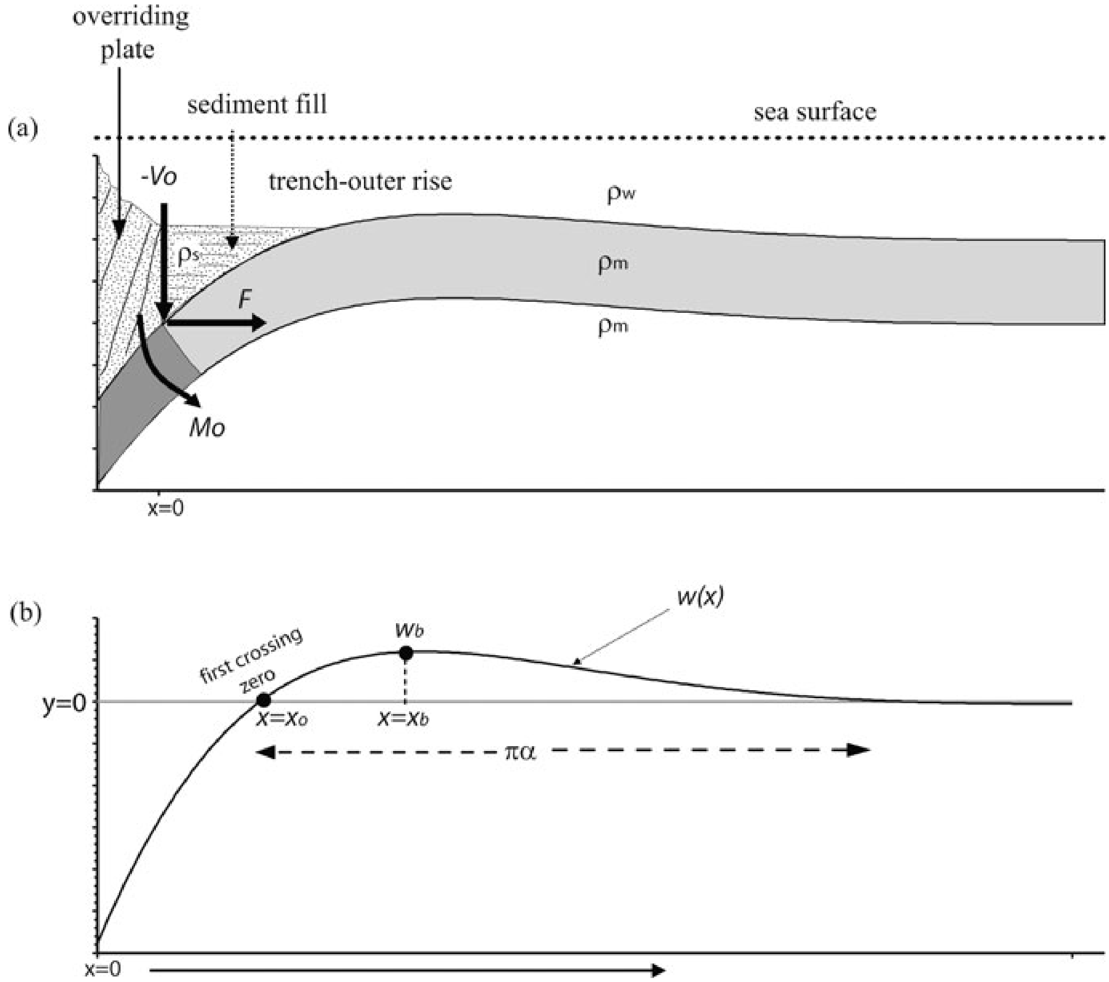

Figure 3. (a) Bending of the lithosphere at an ocean trench due to the applied vertical shear force V_o, horizontal force F and bending moment M_o. ρ_m, ρ_s and ρ_w are the mantle, trench-sediment and water density, respectively. (b) Schematic representation of topography (x_o, x_b, w_b, α) defining the deflection curve $w(x)$.

$$M(x) = -\mathrm{e}^{-x/\alpha}\left[M_o\cos\left(\frac{x}{\alpha}\right) + (V_o\alpha + M_o)\sin\left(\frac{x}{\alpha}\right)\right] \quad (5)$$

$$V(x) = \frac{\mathrm{e}^{-x/\alpha}}{\alpha}\left[-V_o\alpha\cos\left(\frac{x}{\alpha}\right) + (V_o\alpha + 2M_o)\sin\left(\frac{x}{\alpha}\right)\right] \quad (6)$$

where $\alpha = \left(\frac{4D}{(\rho_m-\rho_w)g}\right)^{1/4}$ is the flexural parameter.

To include in our flexural model the effect of sediment loading at the trench basin, we incorporate $q(x) = (\rho_s - \rho_w)gh_s(x)$, where ρ_s and h_s are the sediment density and thickness, respectively. Our approach is to study possible spatial variations in the strength of the lithosphere (i.e. T_e). Therefore, it is convenient to solve (1) and (2) by the method of finite differences which allows D to vary with position along the profile (see Appendix for a detailed description of this method).

3.3 Sediment loading

The flexure of the oceanic lithosphere seaward of trenches may not be only caused by the forearc load associated with the negative buoyancy of the subducting plate, but also by extra loads such as seamounts or sediments. Our finite difference method allows explicit inclusion of extra loads within the term $q(x)$ (eq. 1), and therefore it differs from the most commonly used flexural modelling with $q(x) = 0$ (e.g. Caldwell *et al.* 1976; Parsons & Molnar 1976; Turcotte & Schubert 1982; Levit & Sandwell 1995; Bry & White 2007). As explained in Section 3.1, we avoided extracting bathymetric profiles near seamounts and we focused on the effect of thick sediments in our flexural modelling using seismic reflection data in areas where the trench is sedimented by thick turbidites (profiles 06–09). We assume that the top of the oceanic crust corresponds to the shape of the lithospheric flexure caused by both the forearc shear force and sediment load. The sediment loading is computed as $q(x) = (\rho_s - \rho_w)gh_s(x)$, where the sedimentary thickness $h_s(x)$ is obtained from the seismic reflection profiles. Density values and other parameters are shown in Table 1. Fig. 4(a) shows the sedimentary thickness along profile P08, which represents a large load

Table 1. Values of parameters and constants used in flexural modelling.

Name	Symbol	Value	Unit
Young's modulus	E	70×10^9	Pa
Acceleration due to gravity	g	9.81	m s^{-2}
Poisson's ratio	ν	0.25	
Mantle density	ρ_m	3300	kg m^{-3}
Sediment density	ρ_s	2000	kg m^{-3}
Water density	ρ_w	1030	kg m^{-3}

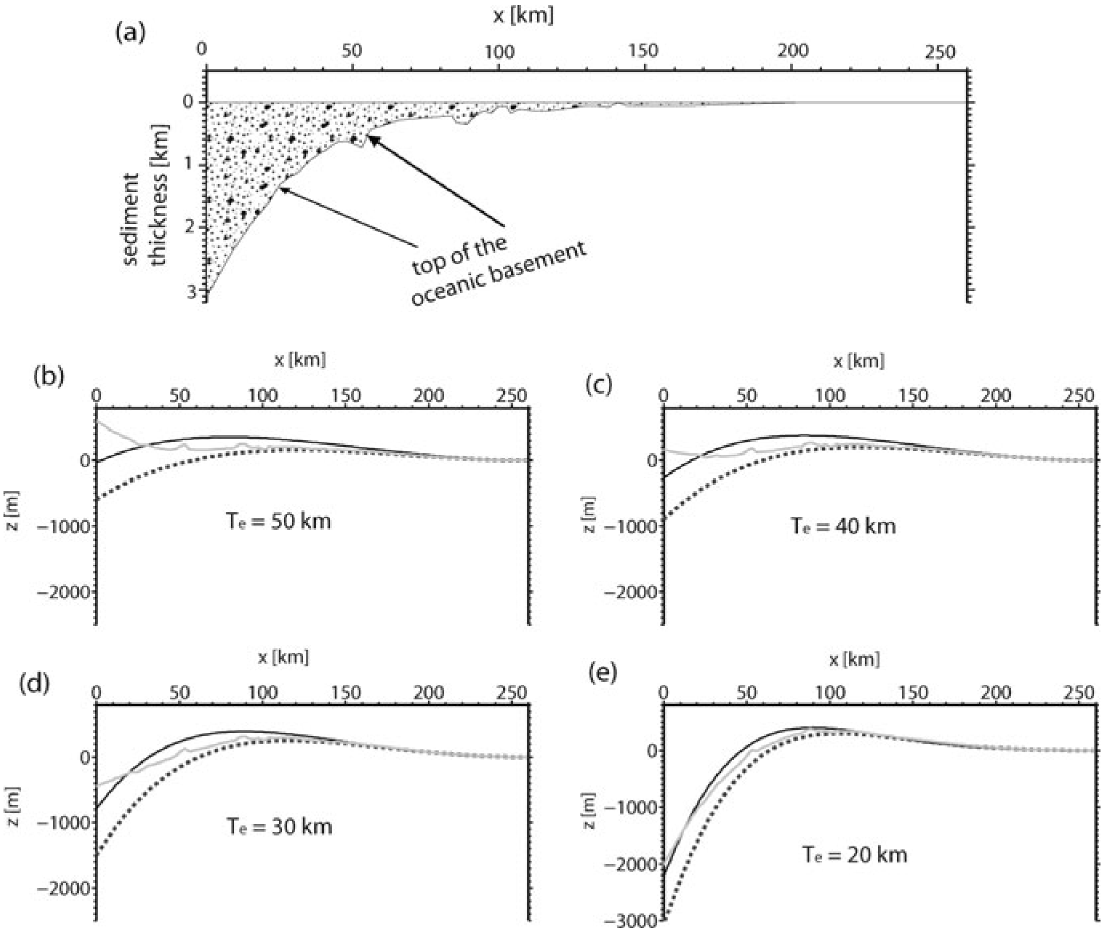

Figure 4. (a) Trench fill thickness $h_s(x)$ which defines a sediment loading $q(x) = (\rho_s - \rho_w)gh_s(x)$ over the lithosphere as shown in Fig. 3(a). (b) Solid curves show the flexure of the lithosphere for an elastic plate with $T_e = 50$ km with a starved trench. The dotted curves show the flexure of the lithosphere with the same elastic thickness but including the sediment loading caused by thick sediments as shown in (a). The grey curves correspond to the flexure of the lithosphere with a removed sediment cover and isostatically corrected this unloading effect on the lithosphere. The same as in (b) for (c)–(e) but with $T_e = 40$, 30 and 20 km, respectively. Numeric values used for calculations are shown in Table 1.

on the oceanic lithosphere that deforms under its weight. Fig. 4(a) also shows the top of the oceanic basement, which is derived from a seismic reflection profile off Isla de Chiloé (Contreras-Reyes *et al.* 2007). The resulting flexure caused by the forearc shear force and sediment load is computed solving (1) with $q(x) = (\rho_s - \rho_w)gh_s(x)$ (Section 3.2).

To explore the effect of sediment loading for different values of T_e on the lithospheric flexure $w(x)$, we compare the flexure for a sedimented and starved trench. $w(x)$ for an elastic plate with constant T_e of 50, 40, 30 and 20 km and empty trench sediments are computed and plotted in Figs 4(b)–(d) (black solid curves). Those curves are compared with the deflection of an elastic plate with identical elastic thicknesses but loaded by the trench fill with sediment thickness $h_s(x)$ as is shown in Fig. 4(a) (dotted curves in Figs 4b–d). The results show that this thick trench fill (Fig. 4a) produces a flexure with extra amplitude $\geq$500 m high and an extra wavelength 50–100 km long. We also test the effect of sediment density ρ_s, and we considered lateral variations in ρ_s as a function of the sedimentary thickness or equivalently as a function of the distance from the trench axis x. For example, sediment density between 0 and 500 m depth was tested with 1700 kg m^{-3} and between 500 and 2200 m with 2100 kg m^{-3}. Results show that $w(x)$ is not significantly sensitive to ρ_s within that range, and 2000 kg m^{-3} is a representative value.

Some authors have removed the sediment cover and isostatically corrected this unloading effect on the lithosphere (e.g. Caldwell *et al.* 1976; Bodine & Watts 1979; Adam *et al.* 2005). Our new flexural modelling approach, in contrast, allows calculation of $w(x)$ for any sediment trench fill distribution and is independent of T_e. To compare these different approaches, we have removed the sediment cover and isostatically corrected this unloading effect on the lithosphere using the correcting term $h_s(x)\frac{(\rho_s-\rho_w)}{(\rho_m-\rho_w)}$ (Caldwell *et al.* 1976; Adam *et al.* 2005). Grey lines in Figs. 4(b)–(d) show the corrected flexure by isostatic unloading which corresponds to the seafloor depths that would have without the sediment load. In some cases the shape of the outer rise was considerably altered by removing the sediments. As we expected, the isostatic correction is only a good approximation for thin elastic thickness ($T_e \leq 20$ km), and it overestimates the rise amplitude $w(x)$ for thick sedimented trenches and elastic plate with $T_e \geq 30$ km. Thus, the thicker T_e and h_s the worse is the isostatic correction. Thus, it is more convenient to explicitly use the sediment load in eq. (1) independent of T_e and the $h_s(x)$-distribution.

In conclusion, the flexure of the lithosphere due to sediment loading is relevant for thickly sedimented trenches causing considerable deflection of the lithosphere. To include this effect we modelled the top of the basement along seismic profiles instead of the bathymetry in regions characterized by sedimented

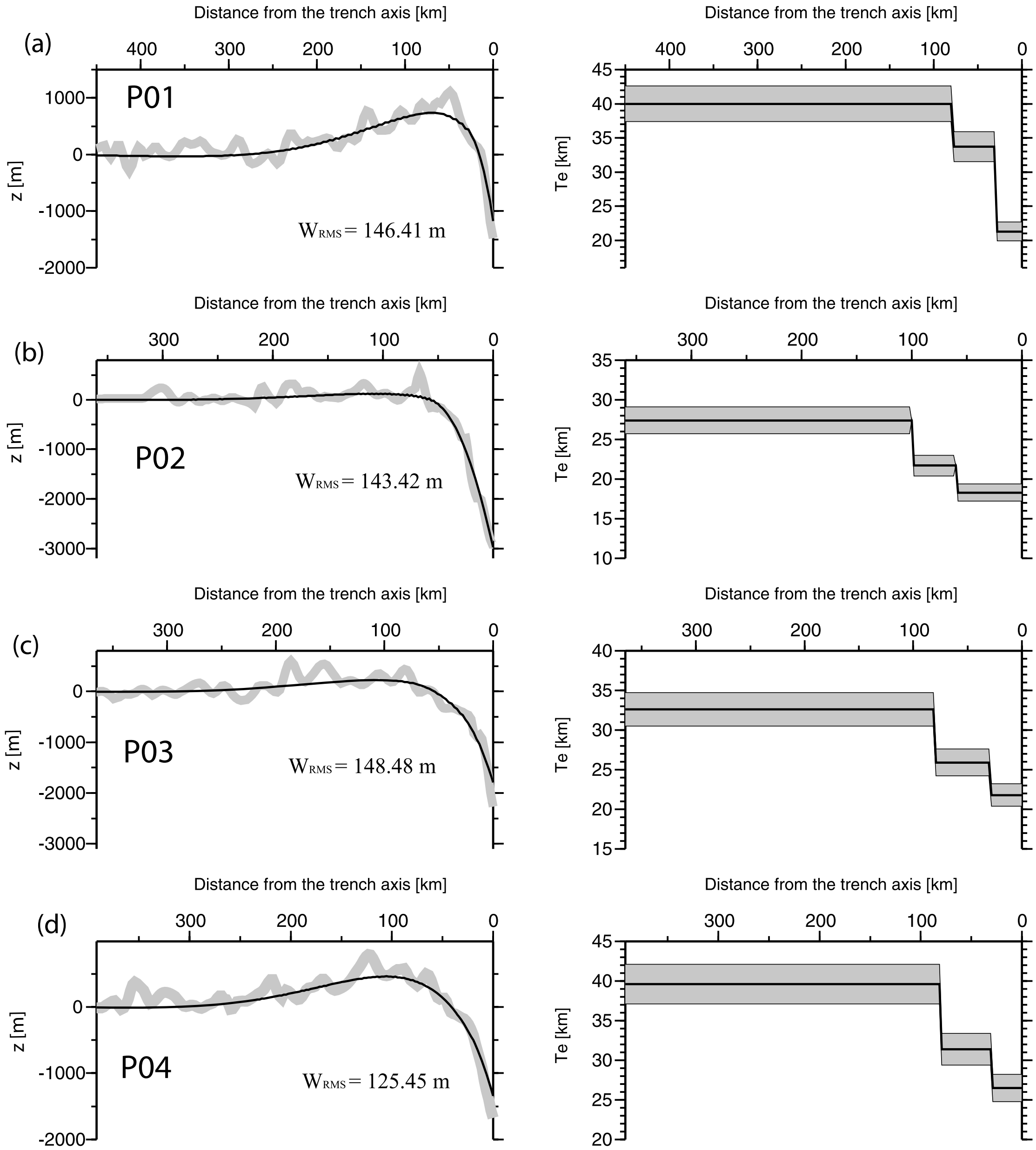

Figure 5. (Left) Topography along profiles P01–P09 (grey line). Profiles are arbitrarily shifted vertically for presentation. Black lines correspond to the average flexure model (see text for details). Profiles are numbered according to the numbering scheme shown in Fig. 1. RMS misfit of flexural models is also shown. (Right) Average $T_e(x)$ models (black line). Grey area denotes the uncertainty-region of $T_e(x)$ (see text for details).

trenches (profiles P06–09) and we included explicitly the sediment load effect in our flexural modelling. The results are shown in Figs 5(f)–(i), where the adjusted flexure (grey curve) corresponds to the top of the oceanic crust obtained from seismic reflection profiles.

3.4 Model uncertainty

The overall objective of the modelling is to establish a set of parameters $\mathbf{m} = (T_e(x), V_o, M_o)$ whose sensitivity characterize the flexural behaviour of the oceanic plate experiencing bending at subduction zones. Therefore, we wish to find the space solution of $\mathbf{m}$ minimizing the squared RMS (root mean square) error $W_{\mathrm{RMS}}(\mathbf{m})$ between the bathymetric data z_i and the predicted flexure $w(\mathbf{m})$

$$W_{\mathrm{RMS}}(\mathbf{m}) = \sqrt{\frac{1}{N}\sum_{i=0}^{N} |w_i(\mathbf{m}) - z_i|^2}, \tag{7}$$

N is the number of points along the profiles and $w(\mathbf{m})$ is computed using eq. (1) with variable flexural rigidity $D(x)$.

The first step consists of finding a reference model $\mathbf{m}_o$, which is constructed by fitting the shape of the outer rise seaward of its peak x_b assuming a constant T_e (Fig. 3). That is, we forward modelled the bathymetric profiles seaward of x_b using (4). Landward from x_b the flexural rigidity can vary freely in a number of segments, which are arbitrarily defined (see Judge & McNutt 1991). Once obtained, a reference model is defined by the parameters $\mathbf{m}_o = (T_e^o(x), V_o^o, M_o^o)$.

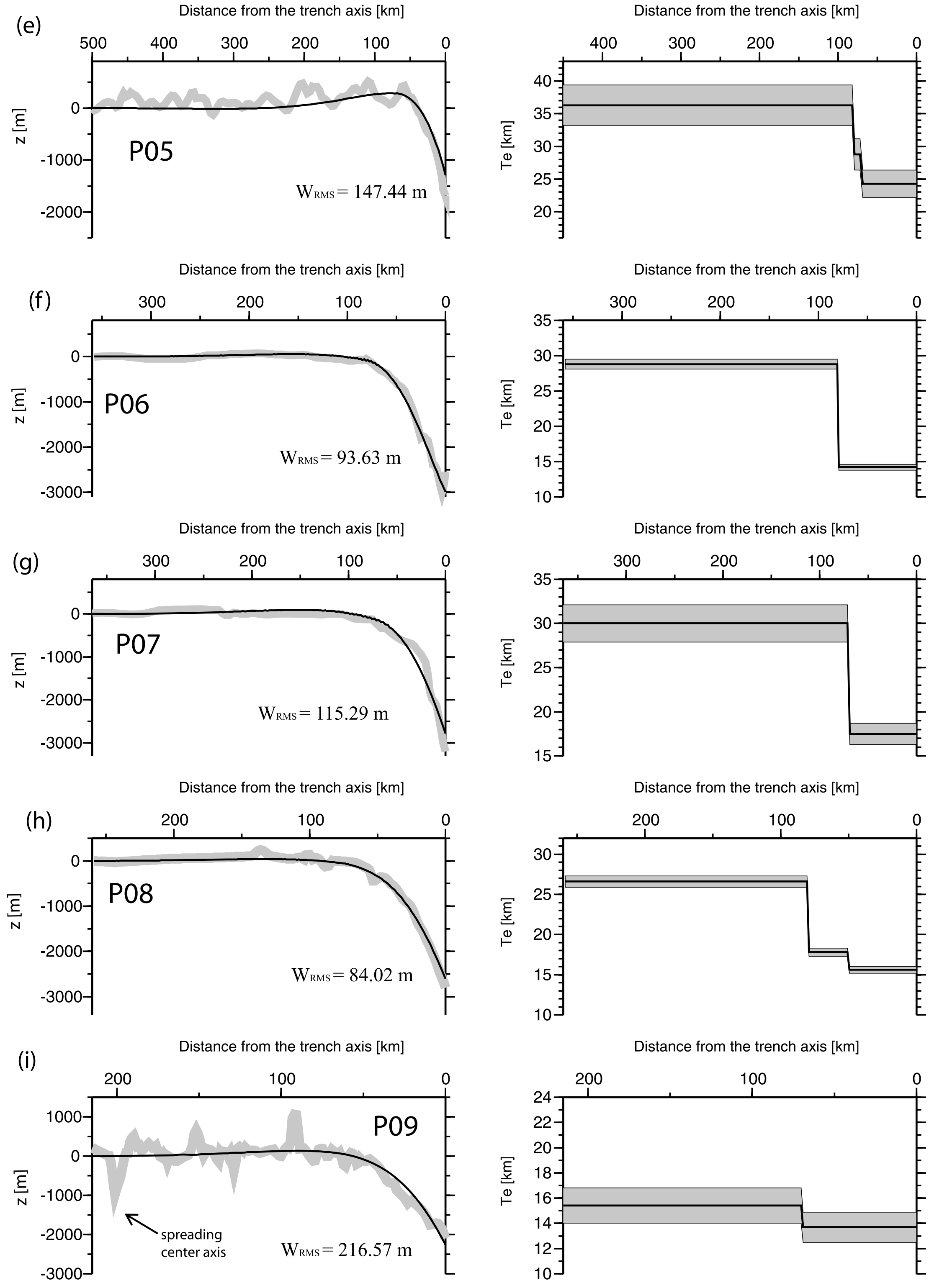

Figure 5. (*Continued.*)

These are perturbed by ±50 per cent, and the root mean square $W_{\mathrm{RMS}}(\mathbf{m}_o + \delta\mathbf{m}_o)$ is calculated to explore the solution space. A reliable solution is achieved if the computed flexure $w(\mathbf{m}_o + \delta\mathbf{m}_o)$ reaches the condition $\chi^2 \leq 1$, where χ^2 is given by

$$\chi^2 = \frac{1}{N}\sum_{i=1}^{N}\left(\frac{w(\mathbf{m})_i - z_i}{\Delta z_i}\right)^2, \tag{8}$$

$\chi^2 = 1$ means that the model error is equal to the data uncertainty Δz_i.

Bathymetric data 'uncertainties' Δz_i are taken to be 1.1 times the minimum value of W_{RMS} (Bry & White 2007). Once a set of solutions that met the condition $\chi^2 \leq 1$ was obtained, we computed the average and standard deviation for each parameter. The standard deviation of $\Delta\mathbf{m} = (\Delta T_e(x), \Delta V_o, \Delta M_o)$ as a function of the average

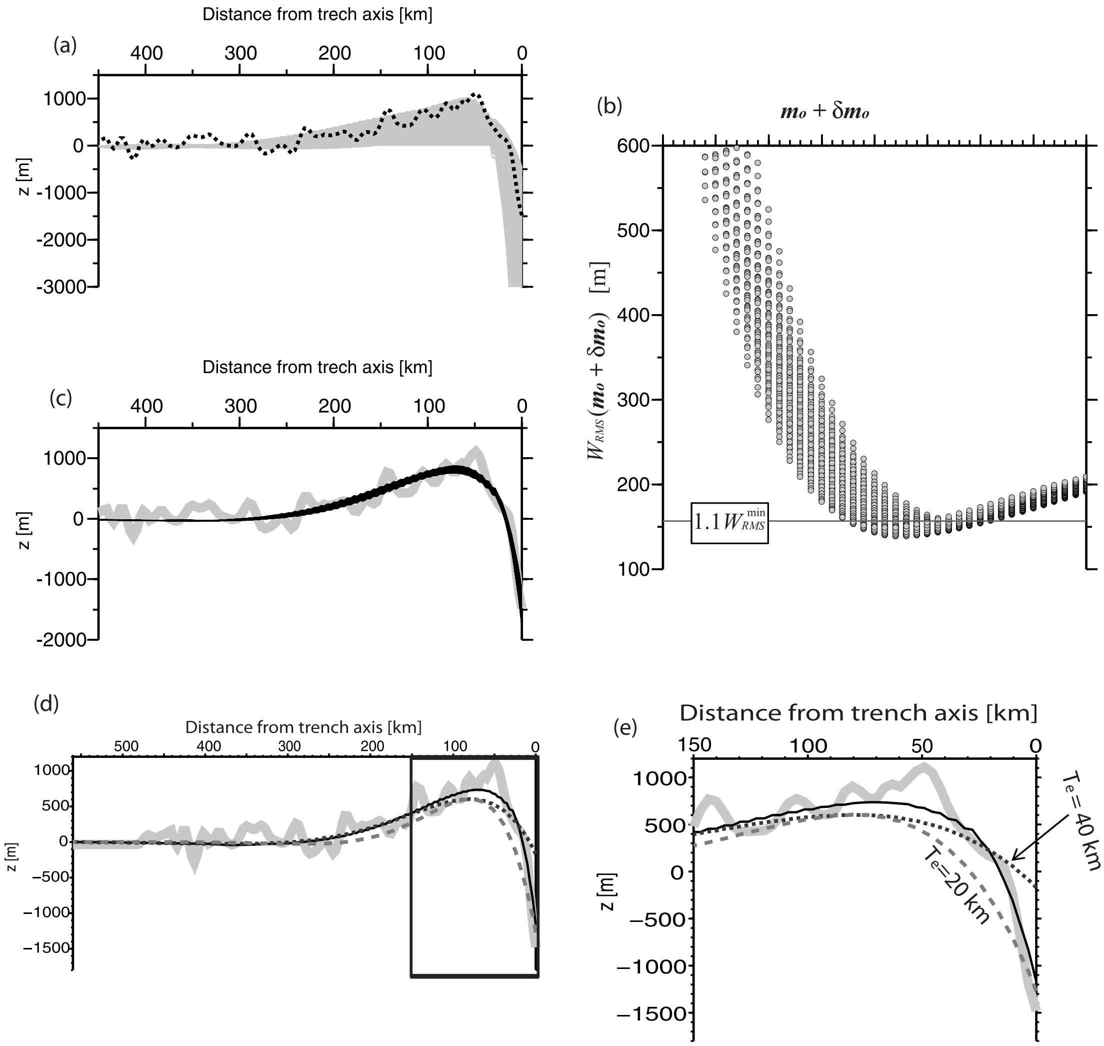

Figure 6. Sensitivity of flexural model to elastic thickness T_e, bending moment M_o and shear force V_o at the trench axis. (a) The dotted line denotes the bathymetric data and the grey area represents the predicted flexural models due to possible variations in the reference parameters (i.e. $w(\mathbf{m} + \delta\mathbf{m}) = w(T_e^o(x) + \delta T_e^o(x), M_o + \delta M_o, V_o + \delta V_o)$). (b) RMS misfit of flexural models $w(\mathbf{m}_o + \delta\mathbf{m}_o)$ as a function of perturbed parameters $\mathbf{m}_o + \delta\mathbf{m}_o$. (c) Grey curve indicates the bathymetric data and black lines represent the solutions $\widehat{\mathbf{m}}$ which reached the condition $\chi^2 \leq 1$. (d) and (e) show the direct comparison of $w(x)$ associated to constant T_e of 20 and 40 km versus a variable $T_e(x)$ which is characterized by a reduction in T_e from 40 to 20 km within 70 km of the trench axis as shown in Fig. 5(a).

estimated parameter ($\overline{T}_e(x)$, $\overline{V}_o$, $\overline{M}_o$) are computed from

$$\Delta T_e(x) = \pm\sqrt{\sum_{i=1}^{N_f} \frac{\left(\widehat{T}_e^i(x) - \overline{T}_e(x)\right)^2}{N_f}}, \tag{9}$$

$$\Delta M_o = \pm\sqrt{\sum_{i=1}^{N_f} \frac{\left(\widehat{M}_o^i - \overline{M}_o\right)^2}{N_f}}, \tag{10}$$

$$\Delta V_o = \pm\sqrt{\sum_{i=1}^{N_f} \frac{\left(\widehat{V}_o^i - \overline{V}_o\right)^2}{N_f}}, \tag{11}$$

where $\widehat{T}_e^i(x)$, $\widehat{M}_o^i$, $\widehat{V}_o^i$ and N_f are the ith estimated parameters and number of solutions which reached the condition $\chi^2 \leq 1$, respectively.

We illustrate the presented strategy in Fig. 6. We plot the calculated flexure $w(\mathbf{m}_o + \delta\mathbf{m}_o)$ associated with perturbations of a reference model $\mathbf{m}_o$ (grey area in Fig. 6a). The RMS misfit of all these possible solutions are plotted in Fig. 6(b) where horizontal variations represent perturbations in $T_e(x)$ while vertical variations represent perturbations in M_o and V_o. We found that there are significant trade-offs between V_o, M_o and, $T_e(x)$ which both moderate the shape of the misfit function and affect the location of its global minimum. The combination of parameters which satisfy the condition $\chi^2 \leq 1$ are selected and their associated flexure $w(x)$ are plotted and compared with the respective bathymetric profile (Fig. 6c). Using these solutions, average values $\overline{T}_e(x)$, $\overline{M}_o$ and $\overline{V}_o$ and their respective standard deviation $\Delta T_e(x)$, ΔM_o and ΔV_o are computed using (9), (10) and (11), respectively. Average distribution and standard deviation for $T_e(x)$ are plotted in Fig. 5 for each studied bathymetric profile. $\overline{M}_o \pm \Delta M_o$ and $\overline{V}_o \pm \Delta V_o$ values are summarized in Table 2.

Most uncertainties in T_e range between $\pm$ 1 and $\pm$ 3 km, whereas ΔM_o and ΔV_o are in a range of $\pm(0.1$–$0.5) \times 10^{16}$ N m and $\pm(0.1$–$0.5) \times 10^{12}$ N, respectively. The estimated uncertainties ΔM_o and V_o are typically less than 20 per cent of the mean value of both

Table 2. Results after Monte Carlo realizations.

Bathymetric profile	Age (Ma)	T_e^M (km)	T_e^m (km)	$M_o(\times 10^{16}$ N m)	$V_o(\times 10^{12}$ N)
P01	48	40.8 ± 2.57	21.1 ± 1.7	2.23 ± 0.18	2.08 ± 0.15
P02	41	27.4 ± 1.68	18.2 ± 1.12	0.37 ± 0.11	1.02 ± 0.12
P03	40	31.7 ± 2.10	22.3 ± 1.4	0.63 ± 0.11	0.24 ± 0.13
P04	39	39.40 ± 2.49	23.5 ± 1.67	1.74 ± 0.19	1.03 ± 0.17
P05	38	36.53 ± 3.08	25.9 ± 2.06	1.04 ± 0.18	0.43 ± 0.17
P06	35	25.88 ± 1.511	14.2 ± 0.49	1.37 ± 0.2	0.19 ± 0.1
P07	30	30.20 ± 2.13	18.5 ± 1.42	0.25 ± 0.10	0.69 ± 0.10
P08	14.5	29.83 ± 0.68	15.8 ± 0.45	0.48 ± 0.04	0.17 ± 0.03
P09	6	15.00 ± 1.40	13.8 ± 1.20	0.29 ± 0.05	0.17 ± 0.09

Note: Age: crustal oceanic age at the trench axis, T_e^M: elastic thickness seaward of the outer rise, T_e^m: elastic thickness at the trench axis, M_o: bending moment at the trench axis and V_o: vertical force at the trench axis are shown.

V_o and M_o, whereas uncertainties of $T_e(x)$ are less than 10 per cent of the average value of $T_e(x)$ (see Fig. 5 and Table 2 for further details).

4 RESULTS

The topographic profile modelling results for the 50–0 Ma oceanic lithosphere at the Chile trench are shown in Fig. 5. The estimated solutions fit the long-wavelength features of the bathymetric data well, whereas, the high-frequency features give an indication of the roughness of the basement topography. The distribution of the derived elastic thicknesses are characterized by a systematic reduction towards the trench for each profile (Fig. 5). The reduction in T_e begins 50–100 km from the trench axis (in the vicinity of the peak of the outer rise) and ranges between 10 and 50 per cent. The reduction in T_e is accompanied by an increase in curvature which suggests inelastic yielding of the lithosphere. The values of T_e found in this study should reflect the amount of thinning that the lithospheric plate is expected to undergo when it is bent to high curvatures.

The adjusted estimates of elastic thickness seaward of the outer rise T_e^M and at the trench axis T_e^m are summarized in Table 2 as a function of the plate age. The results reveal only a weak dependence of elastic thickness on plate age (Fig. 7). This suggests that either T_e does not consistently depend on plate age or that it may also depend on other factors. On the other hand, the flexural wavelength of the outer rise seems to increases with plate age. For example, α is extremely long along P01 (∼300 km) where the plate is oldest, while for plate ages ranging between 45 and 30 Ma α is roughly constant with a value of 150 km (Fig. 7b). For profiles P08 and P09 where the plate ages are 14 and 3 Ma, respectively, α decreases substantially to values of only 30–50 km, which shows a local and narrow 'outer rise' (Fig. 7b). However, this short flexural wavelength is unlikely to be only due to the low flexural rigidity, but also due to the combined effect of relative low T_e and heavy sediment loading in the trench basin.

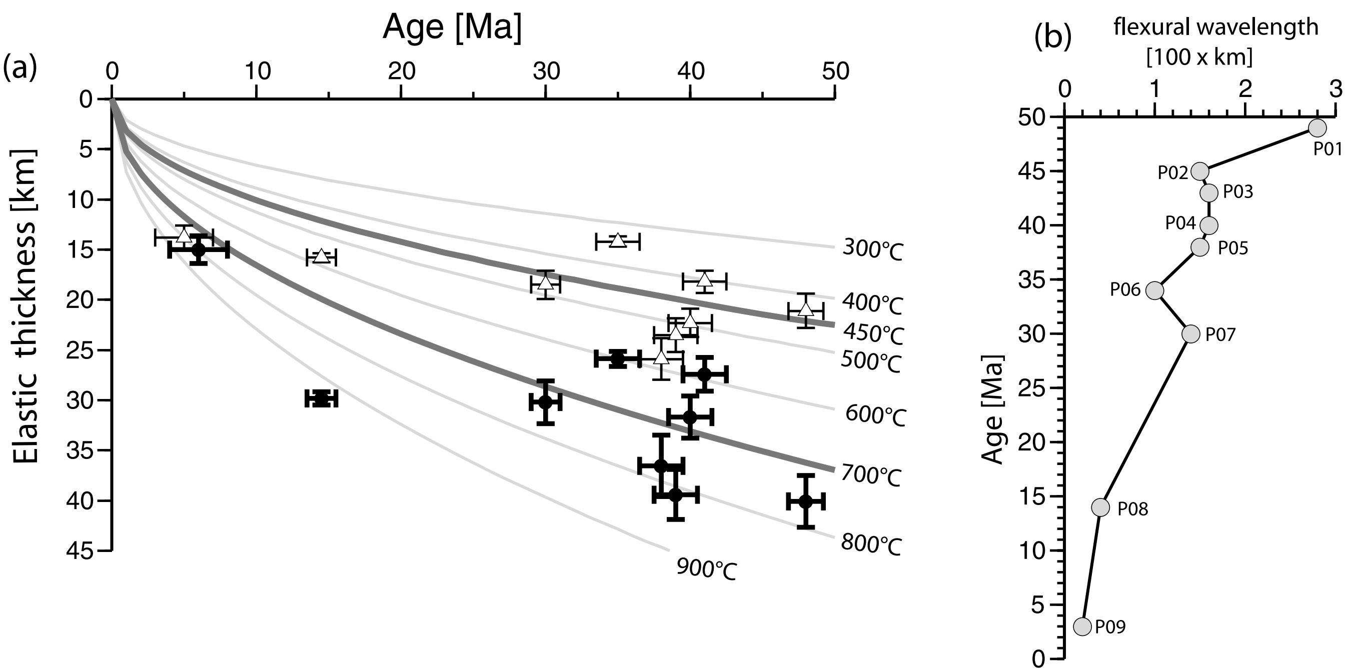

Figure 7. (a) Elastic thickness seaward of the outer rise (black dot-bars) and at the trench axis (white dot-bars) as a function of plate age near the trench. Isotherms are based on the cooling plate model of Parsons & Sclater (1977). Ages of the oceanic crust have been determined from magnetic anomalies using the age grid of Mueller *et al.* (1997). (b) Flexural wavelength of the outer rise off Chile compared to the plate age.

5 DISCUSSION

5.1 Reduction in the elastic thickness of the oceanic lithosphere

5.1.1 *Robustness of flexural results*

To study the robustness of our flexural results, we conducted independent forward modelling seeking elastic models that fit the data. As an example, we show the flexural modelling for profile P01 in Figs 6(d) and (e). The best fit is achieved with the $T_e(x)$ distribution presented in Fig. 5(a) and is characterized by a decrease in T_e from 40 to $\sim$20 km within a narrow region. For comparison, we also plot the flexure associated with a constant elastic thickness of 40 and 20 km. None of these computed flexures accurately predict the steep deflection at the trench axis nor the flexural wavelength. $w(x)$ with $T_e = 20$ km overestimates the deflection and underestimates the flexural wavelength, whereas $w(x)$ with $T_e = 40$ km underestimates the deflection and overestimates the flexural wavelength. We therefore conclude that a reduction in T_e is needed to get enough high amplitude at the trench axis to simulate the steep bend and an appropriate flexural wavelength of the outer rise shown by the bathymetric data. We also test perturbations of M_o and V_o and the results did not change significantly. Similarly, the rest of bathymetric profiles were first examined with a constant T_e and we came to the conclusion that most of the Chilean outer rise region suffers from extremely high curvature and sharp bending, and a reduction in T_e is needed to get high enough amplitudes near the trench axis to mimic the steep bending of the subducting Nazca Plate.

5.1.2 *Elastic and mechanical thicknesses*

If strong bending moments exceed the strength of the plate, it will yield rather than flex, and the lithospheric flexure will be characterized by extremely high curvatures. A reduction in T_e is required to model the high curvatures observed along the studied bathymetric profiles (Fig. 5) and we can consider that the reduction in T_e "simulates" inelastic deformation. Many authors have suggested that elastic thicknesses calculated for plates with such large curvatures underestimate the true mechanical thickness T_m of the plate because inelastic failure effectively reduces the thickness of the layer which can transmit elastic stresses. The true mechanical thickness T_m (i.e. T_e at zero curvature) is a rheological boundary at the base of the high strength mechanical lithosphere (McNutt 1984), and it can be estimated using the ratio of T_m to T_e against curvature (McNutt & Menard 1982). Although the conversion into mechanical thickness has adherents and detractors and further technical analysis of this matter is beyond the scope of this study, we can interpret T_m in this flexural study as T_e seaward of the peak of the outer rise, where the plate curvature is negligible. Thus, the reduction in T_e needed to model the extremely high curvatures near the trench is interpreted as a consequence of inelastic deformation which might be caused by hydro-fracturing weakening mechanisms. Yielding is in accord with seismic reflection and bathymetry data that suggest the presence of normal faults in the outer rise region (see Section 5.2 for further discussion).

5.1.3 *The role of the Young's modulus*

So far, we have quantified the reduction of the flexural rigidity D towards the trench only in terms of the parameter T_e and held constant the Poisson's ratio ν and Young's modulus E. However, reduction in D might also be due to reductions in E, which is directly proportional to D. The Young's modulus can be described in terms of Poisson's ratio, P-wave velocity V_p and density ρ via

$$E = \rho V_p^2 (1 + \nu^2). \tag{12}$$

It is worthwhile to quantify reductions in V_p and ρ and increases in ν due to percolation of fluids within the mantle to check their impact on E and hence on the flexural rigidity. According to Christensen (1996), dry peridotite rocks have typical seismic velocities faster than 8.2 km s^{-1} at 200 MPa (oceanic typical Moho depths). With increasing degree of serpentinization seismic velocities are forced to change to $\sim$4.7 km s^{-1} in serpentinite. Partially serpentinized peridotites have seismic velocities that fall between these limiting values. A typical value for hydrated upper mantle velocity in the Chilean outer rise is $V_p = 7.8$ km s^{-1} (Contreras-Reyes *et al.* 2008a). On the other hand, theory predicts that for increasing fluid-content, the shear wave velocity V_s decreases faster than V_p resulting in the increase in Poisson's ratio (i.e. ν is more sensitive to the presence of fluids than V_p only). A seismic study of the compressional and shear waves in the southern-central Chile outer rise reports a relatively high Poisson's ratio of about 0.28 interpreted in terms of hydrated upper mantle off Isla de Chiloé (Contreras-Reyes *et al.* 2008b). In addition, the infiltration of water also has an impact on the bulk density of mantle rocks, which results in a reduction in ρ. For offshore Antofagasta (Chile at $\sim$23°S), Ranero & Sallares (2004) reported a low mantle density of 3150 kg m^{-3} which was interpreted in terms of water percolation leading to mineral alteration and hydration of the mantle. If we consider these values of $V_p = 7.8$ km s^{-1}, $\nu = 0.28$ and $\rho = 3150$ kg m^{-3} as 'hydrated' upper mantle against 'normal' unaltered upper mantle seaward of the outer rise with $V_p = 8.1$ km s^{-1}, $\nu = 0.25$ and $\rho = 3300$ kg m^{-3} we may infer that E is reduced by about 17 per cent implying a reduction in D of $\sim$16 per cent (assuming a constant elastic thickness of 30 km). On the other hand, if we keep E fixed then a small reduction in T_e from 30 to 28 km ($\sim$7 per cent) results in a drastic reduction in the flexural rigidity by the same amount ($\sim$16 per cent), and hence D is about three times more sensitive to T_e than E. So, we conclude that the reduction in the flexural rigidity towards the trench detected in this study is mainly due to a decrease in T_e rather than E.

5.2 Plate weakening mechanisms

The large curvatures and reduction in T_e observed along the Chile trench suggest that high strains develop due to strong bending, which exceeds the yield strength of the lithosphere resulting in inelastic deformation and the loss of strength of the lithosphere. A large portion of such high strains is associated with brittle deformation in the upper extensional part of the lithosphere as is evidenced by horst and graben structures and numerous extensional faults imaged by seismic reflection lines and swath bathymetric data (Ranero *et al.* 2005). Normal faults exist along the entire Chile trench, with an average offset of several hundred metres except in northern Chile where offsets of over a kilometre exist. South of the JFR the fractured oceanic basement in the outer rise region is masked by thick sediments. However, seismic reflection data revealed outer rise bending-related faults cutting at least 6 km into the uppermost mantle (Grevemeyer *et al.* 2005). Seawater may enter through these fractures into the crust and upper mantle resulting in the serpentinization of the mantle (Ranero *et al.* 2005). Hydration and fracturing of the upper mantle is also indicated by a decrease in mantle velocities below the outer rise as seen off Antofagasta at 22°S (Ranero & Sallares 2004), off Valparaíso at 33°S (Kopp

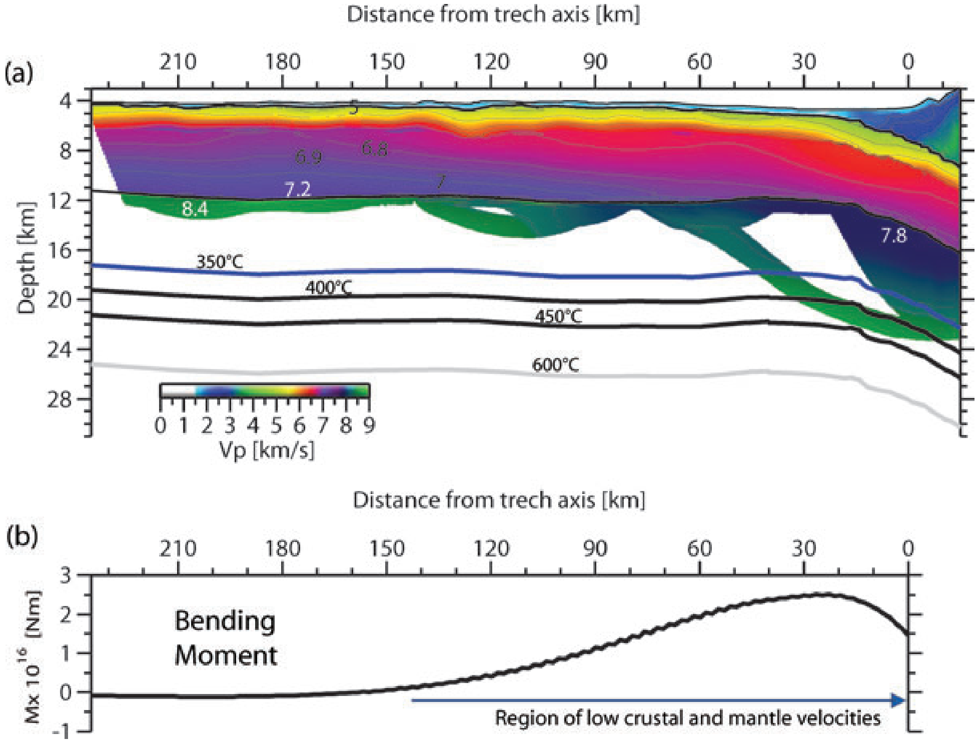

Figure 8. (a) Velocity-depth model off Peninsula de Arauco at $\sim$38°S modified from Contreras-Reyes *et al.* (2008a). Isotherm computations are based on the cooling of a semi-infinite half-space model (Turcotte & Schubert 1982). (b) Bending Moment $M(x)$ obtained along P07 from flexural modelling. Note that reduction in crustal and mantle velocities are fairly coincident with the increase in bending moment.

et al. 2004), off Arauco at 38°S (Contreras-Reyes *et al.* 2008a) and offshore Isla de Chiloé at 43°S (Contreras-Reyes *et al.* 2007). The increase in fluid pore-pressure and fracturing degree are efficient mechanisms for weakening of the lithosphere resulting first in a weakening of molecular bonds within crystals and second in a reduction of the confining pressure and hence the reduction in the overall rock strength (e.g. Brace & Kohlstedt 1980). A previous spectral isostatic study also inferred significant weakening of the oceanic Nazca Plate approaching the trench in terms of low T_e values (Tassara *et al.* 2007). They further speculated that along-strike variation in the strength of subducting plate could be related to variations in the degree of hydration and serpentinization of the oceanic upper mantle.

Contreras-Reyes *et al.* (2008a) reported a region of low crustal and mantle velocities in the trench outer rise region off southern Arauco at 38°S interpreted as a fractured and hydrated lithosphere. The low-velocity zone extends through $\sim$10 km of the uppermost mantle and is coincident with the 450°C isotherm (Fig. 8). They further discuss that the maximum depth of water infiltration is controlled by the neutral surface because fluids cannot penetrate into the compressional regime underneath the neutral surface. Seno & Yamanaka (1996) studied focal mechanisms earthquake data and conclude that a good proxy for the neutral surface corresponds to the isotherm of 450 °C, which is roughly coincident with the limit of the low-velocity zone shown in Fig. 8. Thus, the brittle lithosphere could be described in terms of an upper extensional part which may be weakened by hydration and fracturing simultaneously, and a dry compressional part affected by faulting as is shown by compressional events at depths larger than 20 km depths (Christensen & Ruff 1983). Fig. 8 shows the predicted bending moment obtained by the P07 modelling profile compared with the projected seismic profile published by Contreras-Reyes *et al.* (2008a). The maximum depth of low mantle velocities increases towards the trench reaching its maximum a few kilometres seaward of the trench. It is striking that as the bending moment increases the depth limit for hydration also increases, suggesting a progressively deeper penetration of faults towards the trench, and hence perhaps a large degree of plate weakening.

5.3 3-D effects

Bathymetric profile P01 (Fig. 5a) is quite striking because it has a very high peak of the outer rise ($w_b \sim 650$ m) larger than observed in most outer rises. This high peak occurs in the region of the Arica bend, where the strike of the trench axis changes over 45° within 200 km. Here the sharp turn in the trench may be affecting the shape and amplitude of the outer rise (Judge & McNutt 1991). Consequently, the predicted maximum bending moment and flexural wavelength from our flexural model are also large (15–20×10^{16} N m and $\sim$300 km, respectively). It is important to point out that the high amplitude and bending moment is likely associated to 3-D deformation of the outer rise in the region of the Arica bend, where the flexural parameters may be overestimated from our 1-D flexural modelling. Three dimensional effects may induce tearing or a substantial degree of twisting of the subducting plate (Judge & McNutt 1991).

5.4 Relation of T_e and plate age

It is widely accepted that the elastic thickness increases as the oceanic lithosphere becomes older, cooler and stronger away from the spreading centre (e.g. Watts 1978; Caldwell & Turcotte 1979; McNutt & Menard 1982). When a plate is loaded, its flexural response is a function of its strength at the time of loading. Thus, T_e is most often interpreted as the depth to an isotherm. Elastic plate studies indicate two distinct populations of T_e: those for seamounts that approximate the 200–400 °C isotherm (Watts *et al.* 1980) and those for trenches that approximate the 600°–800°C isotherms (Caldwell & Turcotte 1979; McNutt 1984; McAdoo *et al.* 1985) according to the cooling plate model of Parsons & Sclater (1977) which delimits the base of the mechanical lithosphere. However, other authors have recently claimed no consistent increase in T_e as a function of plate age (Bry & White 2007). Inconsistencies have usually been attributed to thermal anomalies such as thermal resetting McNutt & Menard (1982) or inadequacy of the purely elastic plate model for describing the mechanical behaviour of the oceanic lithosphere (McNutt & Menard 1982; Turcotte *et al.* 1978).

Our new elastic results show no systematic increase in T_e with plate age suggesting either T_e does not depend on plate age or it is influenced by other factors such as plate-loading history and the degree of weakening. Weakening represents the plate's memory of previous deformation, that influence subsequent stress distributions and new deformation (Mueller *et al.* 1996). Unfortunately, the loading history and the degree of inelasticity that the lithosphere has undergone are largely uncertain.

One could expect that if the plate is older and therefore more rigid it should be able to resist weakening more effectively. However, several examples in Fig. 5 shows that reduction in T_e for plate ages older than 40 Ma is up to 50 per cent, which is larger than the reduction in T_e for plate ages younger than 30 Ma. We interpret this large reduction in T_e for older plate in terms of brittle failure processes which likely act deeper for older plates. That is, because the transition-depth from brittle to ductile within the lithosphere increases as the age increases (e.g. Mueller *et al.* 1996) then the volume available for fracturing and hydration also increases. We speculate that this critical transition-depth would be directly related to hydro-fracturing and hence weakening. This may explain why old plates may experience a larger amount of weakening than young plates. Young plates, in contrast, are characterized by a shallower brittle–ductile transition, and therefore the amount of brittle deformation and weakening that they may be expected to suffer owing to bending stresses is smaller than older and colder plates. The latter shows a complex relationship between T_e and plate age. On the one hand, old plates are thicker and more capable of supporting tectonic stresses, but on the other hand, older and colder plates are likely to experience more weakening and hence a more pronounced reduction in T_e.

6 CONCLUSIONS

This work leads to the following conclusions:

(i) The results show a systematic reduction in T_e towards the trench reaching values up to 50 per cent thinner than seaward of the outer rise. The reduction in T_e is coincident with high plate curvatures, strong bending moments, pervasive fracturing and faulting of the oceanic basement as is imaged by high resolution bathymetry data and reduction of crustal and mantle seismic velocities.

(ii) The reduction in T_e and hence weakening of the oceanic lithosphere is interpreted to be caused by fracturing and a likely increase of fluid-pore pressure in the outer rise region, where hydration may be an effective plate weakening mechanism only in the extensional regime of the plate where the water infiltration is confined.

(iii) The results indicate that it is difficult to relate the strength of subducting plates to their age and old plates appears to experience more weakening than young plates.

ACKNOWLEDGMENTS

The authors thank Mark Falvey and Dave Rahn for comments on the English. Fruitful discussions with Andrés Tassara, Anthony B. Watts and Mark A. Richards are greatly appreciated. Eduardo Contreras-Reyes acknowledges the support of the Chilean Fondo Nacional de Desarrollo Científico y Tecnológico (FONDECYT), grant 11090009. Axel Osses was partially supported by FONDECYT-Conicyt 1061263. The authors thank the useful comments and suggestions from the Editor, Cindy Ebinger, and two anonymous reviewers.

REFERENCES

Adam, C., Vidal, V. & Bonneville, A., 2005. MiFil: A method to characterize seafloor swells with application to the south central Pacific, *Geochem. Geophys. Geosyst.,* **6,** Q01003, doi:10.1029/2004GC000814.

Angermann, D., Klotz, J. & Reigber, C., 1999. Space-geodetic estimation of the Nazca-South America Euler vector, *Earth planet. Sci. Lett.,* **171**(3), 329–334.

Bangs, N.L. & Cande, S.C., 1997. Episodic development of a convergent margin inferred from structures and processes along the Southern Chile margin. *Tectonics,* **16,** 489–503.

Billen, M.I. & Gurnis, M., 2005. Constraints on subducting plate strength within the Kermadec trench, *J. geophys. Res.,* **110,** B05407, doi:10.1029/2004JB003308.

Bodine, J.H. & Watts, A.B., 1979. On the lithospheric flexure seaward of the Bonin and Mariana Trenches, *Earth planet. Sci. Lett.,* **43,** 132–148.

Bodine, J.H., Steckler, M.S. & Watts, A.B., 1981. Observations of flexure and the rheology of the oceanic lithosphere, *J. geophys. Res.,* **86**(B5), 3695–3707.

Bourgois, J., Guivel, C., Lagabrielle, Y., Calmus, T., Boulègue, J. & Daux, V., 2000. Glacial–interglacial trench supply variation, spreading-ridge subduction, and feedback controls on the Andean margin development at the Chile triple junction area (45–48°S), *J. geophys. Res.,* **105**(B4), 8355–8386.

Brace, W.F. & Kohlstedt, D.L., 1980. Limits on lithospheric stress imposed by laboratory experiments, *J. geophys. Res.,* **85**(B11), 6248–6252.

Bry, M. & White, N., 2007. Reappraising elastic thickness variation at oceanic trenches, *J. geophys. Res.,* **112,** B08414, doi:10.1029/2005JB004190.

Caldwell, J.G. & Turcotte, D.L., 1979. Dependence of the thickness of the elastic oceanic lithosphere on age, *J. geophys. Res.,* **84,** 7572–7576.

Caldwell, J.G., Haxby, W.F., Karig, D.E. & Turcotte, D.L., 1976. On the applicability of a universal elastic trench profile, *Earth planet. Sci. Lett.,* **31,** 239–246.

Capitanio, F.A., Morra, G. & Goes, S., 2009. Dynamics of plate bending at the trench and slab plate coupling, *Geochem. Geophys. Geosyst.,* **10,** Q04002, doi:10.1029/2008GC002348.

Christensen, N.I., 1996. Poisson's ratio and crustal seismology, *J. geophys. Res.,* **101,** 3139–3156, doi:10.1029/95JB03446.

Christensen, D.H. & Ruff, L.J., 1983. Outer-rise earthquakes and seismic coupling, *Geophys. Res. Lett.,* **10,** 697–700.

Contreras-Reyes, E., Grevemeyer, I., Flueh, E.R., Scherwath, M. & Heesemann, M., 2007. Alteration of the subducting oceanic lithosphere at the southern central Chile trench-outer rise, *Geochem. Geophys. Geosyst.,* **8,** Q07003, doi:10.1029/2007GC001632.

Contreras-Reyes, E., Grevemeyer, I., Flueh, E.R. & Reichert, C., 2008a. Upper lithospheric structure of the subduction zone offshore southern Arauco Peninsula, Chile at ∼38°S, *J. geophys. Res.,* **113,** B07303, doi:10.1029/2007JB005569.

Contreras-Reyes, E., Grevemeyer, I., Flueh, E.R., Scherwath, M. & Bialas, J., 2008b. Effect of trench-outer rise bending-related faulting on seismic Poisson's ratio and mantle anisotropy: a case study offshore of Southern Central Chile, *Geophys. J. Int.,* **173,** 142–156, doi:10.1111/j.1365-246X.2008.03716.x.

Diaz-Naveas, L, J., 1999. Sediment subduction and accretion at the Chilean convergent margin between 35° und 40°S, *PhD thesis*, Ch.-A.-Universitaet, Kiel, Germany.

DeMets, C., Gordon, R.G., Argus, D.F. & Stein, S., 1990. Current plate motions, *Geophys. J. Int.,* **101,** 425–478.

Flueh, E.R. & Grevemeyer, I., 2005. TIPTEQ SONNE Cruise SO-181 (Eds.), from the Incoming Plate to mega Thrust EarthQuakes, Geomar Report 102, Geomar, Kiel, Germany.

Flueh, E.R., Kopp, H. & Schreckenberger, B. (eds), 2002. Subduction processes off Chile. Cruise Report, Geomar.

Goetze, C. & Evans, B., 1979. Stress and temperature in the bending lithosphere as constrained by experimental rock mechanics, *Geophys. J. R. astr. Soc.,* **59,** 463–478.

Grevemeyer, I., Kaul, N., Diaz-Naveas, J.L., Villinger, H., Ranero, C.R. & Reichert, C., 2005. Heat flow and bending-related faulting at subduction trenches: case studies offshore of Nicaragua and Central Chile, *Earth planet. Sci. Let.,* **236,** 238–248.

Hanks, T.C., 1971. The Kuril trench-Hokkaido Rise system: large shallow earthquakes and simple models of deformation, *Geophys. J. R. astr. Soc.,* **23,** 173.

Harris, R. & Chapman, D., 1994. A comparison of mechanical thickness estimates from trough and seamount loading in the southeastern Gulf of Alaska, *J. geophys. Res.,* **99**(B5), 9297–9317.

Herron, E.M., Cande, S.C. & Hall, B.R., 1981. An active spreading centre collides with a subduction zone, a geophysical survey of the Chile margin triple junction, *Geol. Soc. Am. Memories, G* **154,** 683–701.

Ivandic, M., Grevemeyer, I., Bialas, J. & Petersen, C.J., 2010. Serpentinization in the trench-outer rise region offshore of Nicaragua: constraints from seismic refraction and wide-angle data, *Geophys. J. Int.,* **180**(3), 1253, doi:10.1111/j.1365-246X.2009.04474.x.

Jordan, T.A. & Watts, A.B., 2005. Gravity anomalies, flexure and the elastic thickness structure of the Indian-Eurasia collisional system, *Earth planet. Sci. Lett.,* **236,** 732–750.

Judge, A.V. & McNutt, M.K., 1991. The Relationship Between Plate Curvature and Elastic Plate Thickness: A Study of the Peru-Chile Trench, *J. geophys. Res.,* **96**(B10), 16 625–16 639.

Kopp, H., Flueh, E.R., Papenberg, C. & Klaeschen, D., 2004. Seismic investigations of the O'Higgins Seamount Group and Juan Fernandez Ridge: aseismic ridge emplacement and lithosphere hydration, *Tectonics,* **23,** TC2009, doi:10.1029/2003TC001590.

Levitt, D.A. & Sandwell, D.T., 1995. Lithospheric bending at subduction zones based on depth soundings and satellite gravity, *J. geophys. Res.,* **100,** 379–400.

Masson, D.G., 1991. Fault patterns at outer trench walls, *Mar. geophys. Res.,* **13,** 209–225.

McAdoo, D., 1982. On the compensation of geoid anomalies due to subducting slabs, *J. geophys. Res.,* **87**(B10), 8684–8692.

McAdoo, D.C., Caldwell, J.G. & Turcotte, D.L., 1978. On the elastic-perfectly plastic bending of the lithosphere under generalized loading with application to the Kuril Trench, *Geophys. J. R. astr. Soc.,* **54,** 11–26.

McAdoo, D.C., Martin, C.F. & Poulose, S., 1985. Seasat observations of flexure: Evidence for a strong lithosphere, *Tectonophysics,* **116,** 209–222.

McNutt, M.K., 1984. Lithospheric flexure and thermal anomalies, *J. geophys. Res.,* **89,** 11 180–11 194.

McNutt, M.K. & Menard, H.W., 1982. Constraints on yield strength in the oceanic lithosphere derived from observations of flexure, *Geophys. J. R. astr. Soc.,* **71,** 363–394.

Molnar, P. & Atwater, T., 1978. Interarc spreading and cordilleran tectonics as alternates related to the age of subducted oceanic lithosphere, *Earth planet. Sci. Lett.,* **41,** 330–340.

Mueller, S., Choy, G.L. & Spence, W., 1996. Inelastic models of lithospheric stress-I. Theory and application to outer-rise plate deformation, *Geophys. J. Int.,* **125**(1), 39–53 doi:10.1111/j.1365-246X.1996.tb06533.x.

Mueller, R.D., Roest, W.R., Royer, J.-Y., Gahagan, L.M. & Sclater, J.G., 1997. Digital isochrons of the world's ocean floor, *J. geophys. Res.,* **102**(B2), 3211–3214.

Parsons, B. & Molnar, P., 1976. The origin of outer topographic rises associated with trenches, *Geophys J. R. astr. Soc.,* **45,** 707–712.

Parsons, B. & Sclater, J.G., 1977. An analysis of the variation of oceanic floor bathymetry and heat flow with age, *J. geophys. Res.,* **82,** 803–827.

Ranalli, G., 1994. Nonlinear flexure and equivalent mechanical thickness of the lithosphere, *Tectonophysics,* **240,** 107–114.

Ranero, C.R. & Sallares, V., 2004. Geophysical evidence for alteration of the crust and mantle of the Nazca Plate during bending at the north Chile trench, *Geology,* **32,** 549–552.

Ranero, C.R., Villaseor, A., Phipps Morgan, J. & Weinrebe, W., 2005. Relationship between bend-faulting at trenches and intermediate-depth seismicity, *Geochem. Geophys. Geosyst.,* **6,** Q12002, doi:10.1029/2005GC000997.

Sandwell, D.T. & Smith, W.H.F., 1997. Marine gravity anomaly from Geosat and ERS-1 satellite altimetry, *J. geophys. Res.,* **102,** 10039–10054.

Scherwath, M., Flueh, E., Grevemeyer, I., Tilmann, F., Contreras-Reyes, E. & Weinrebe, W., 2006. Investigating subduction zone processes in Chile, *Eos Trans. AGU,* **87**(27), 265, doi:10.1029/2006EO270001.

Scherwath, M., Contreras-Reyes, E., Flueh, E.R., Grevemeyer, I., Krabbenhoeft, A., Papenberg, C., Petersen, C.J. & Weinrebe, R.W., 2009. Deep lithospheric structures along the southern central Chile margin from wide-angle P-wave modelling, *Geophys. J. Int.,* **179**(1), 579–600.

Seno, T. & Yamanaka, Y., 1996. Double seismic zones, compressional deep trench-outer rise events and superplumes, in *Subduction: Top to Bottom,* Geophys. Monogr. Ser., Vol. 96, pp. 347–355, eds Bebout, G. et al., AGU, Washington, DC.

Tassara, A., Swain, C., Hackney, R. & Kirby, J., 2007. Elastic thickness structure of South America estimated using wavelets and satellite-derived gravity data, *Earth planet. Sci. Lett.,* **253**(1–2), 17–36.

Tebbens, S.F., Cande, S.C., Kovacs, L., Parra, J.C., LaBrecque, J.L. & Vergara, H., 1997. The Chile ridge: A tectonic framework, *J. geophys. Res.,* **102**(B6), 12 035–12 060, doi: 10.1029/96JB02581.

Thornburg, T.M., Kulm, D.M. & Hussong, D.M., 1990. Submarine-fan development in the southern Chile trench: a dynamic interplay of tectonics and sedimentation, *Geol. soc. Am. Bull.,* **102,** 1658–1680.

Tilmann, F.J., Grevemeyer, I., Flueh, E.R., Dahm, T. & Gossler, J., 2008. Seismicity in the outer rise offshore southern Chile: indication of fluid effects in crust and mantle, *Earth planet. Sci. Lett.,* **269,** 41–55, doi:10.1016/j.epsl.2008.01.044.

Turcotte, D. & Schubert, G., 1982. *Geodynamics-Applications of Continuum Physics to Geological Problems,* John Wiley, Hoboken, NJ.

Turcotte, D.L., McAdoo, D.C. & Caldwell, J.G., 1978. An elastic-perfectly plastic analysis of the bending of the lithosphere at a trench, *Tectonophysics.,* **47,** 193–208.

Voelker, D.M., Wiedicke, S., Ladage, C., Gaedicke, C., Reichert, C., Rauch, K., Kramer, W. & Heubeck, C., 2006. Latitudinal variation in sedimentary processes in the Peru-Chile Trench off Central Chile, in *The Andes—Active Subduction Orogeny,* pp. 193–216, eds Oncken, O. et al., Springer Press, Berlin.

von Huene, R., Corvalán, J., Flueh, E.R., Hinz, K., Korstgard, J., Ranero, C.R., Weinrebe, W. and CONDOR Scientists, 1997. Tectonic control of the subducting Juan Fernández Ridge on the Andean margin near Valparaiso, Chile, *Tectonics,* **16**(3), 474–488, doi:10.1029/96TC03703.

Watts, A.B., 1978. An analysis of isostasy in the worlds oceans: 1. Hawaiian-Emperor seamount Chain, *J. geophys. Res.,* **83,** 5989–6004.

Watts, A.B. & Talwani, M., 1974. Gravity anomalies seaward of deep-sea trenches and their tectonic implications, *J.R. astr. Soc.,* **36,** 57–92.

Watts, A.B., Bodine, J.H. & Steckler, M.S., 1980. Observations of Flexure and the State of Stress in the Oceanic Lithosphere, *J. geophys. Res.,* **85**(B11), 6369–6376.

APPENDIX A: FLEXURAL MODELLING

The flexure of a rigid lithosphere overlying a fluid-weak asthenosphere is governed by equation (1), which can be re-written with variable elastic thickness for $x \in [0, L]$ in the form of a first-order system with variable coefficients as follows:

$$\frac{\mathrm{d}w}{\mathrm{d}x} = z, \tag{A1}$$

$$\frac{\mathrm{d}z}{\mathrm{d}x} = -D^{-1}(x)M, \tag{A2}$$

$$\frac{\mathrm{d}M}{\mathrm{d}x} = R, \tag{A3}$$

$$\frac{\mathrm{d}R}{\mathrm{d}x} = -F(x)D^{-1}(x)M + \Delta\rho g w - q(x), \tag{A4}$$

where $\Delta\rho = \rho_{\mathrm{m}} - \rho_{\mathrm{w}}$ (see Section 3.2 for details). Eqs (A1)–(A4) can be re-written in the condensed form as follows:

$$\frac{\mathrm{d}S}{\mathrm{d}x} + P(x)S = Q(x), \tag{A5}$$

where $S = (w, z, M, R)^t$ is the augmented state, $Q(x) = (-q, 0, 0, 0)^t$ is the right-hand side, and

$$P(x) = \begin{pmatrix} 0 & -1 & 0 & 0 \\ 0 & 0 & D^{-1}(x) & 0 \\ 0 & 0 & 0 & -1 \\ -\Delta\rho & 0 & F(x)D^{-1}(x) & 0 \end{pmatrix} \tag{A6}$$

The eq. (A5) are discretized using centred differences at N equidistant points $x_1, \ldots, x_N$ in $[0, L]$, that is $x_n = (n-1)\Delta x$, $\Delta x = L/(N-1)$, $n = 1, \ldots, N$. If we denote by S_n the corresponding approximation of $S(x_n)$, and $P_n = P(x_n)$, $Q_n = Q(x_n)$, then the centred scheme reads

$$\frac{S_{n+1} - S_n}{2\Delta x} + P_n S_n = Q_n, \qquad n = 2, \ldots, N-1.$$

That is $-S_{n-1} + 2\Delta x P_n S_n + S_{n+1} = -2\Delta x Q_n$, so if we arrange the unknowns as $(S_1, S_2, \ldots, S_N)$ the corresponding finite difference system is a $4N \times 4N$ tridiagonal block matrix. At $x_1 = 0$ and $x_N = L$ we prescribe the following boundary conditions (Section 3)

$$w_N = 0,\ z_N = 0, \quad M_1 = M_{\mathrm{o}},\ R_1 = V_{\mathrm{o}} + F(0)z_1.$$

We need two other equations at the right side of the interval $[0, L]$ that we establish using left differences at x_N

$$\frac{z_N - z_{N-1}}{\Delta x} + D(L)^{-1}M_N = 0, \quad \frac{M_N - M_{N-1}}{\Delta x} - R_N = 0$$

and two other equations at the left side of the interval $[0, L]$ that we re-write as right differences at x_1

$$\frac{z_2 - z_1}{\Delta x} + D(0)^{-1}M_1 = 0, \quad \frac{w_2 - w_1}{\Delta x} - z_1 = 0$$

with this, we have as many unknowns ($4N$) as equations: $4(N-2)$ centred differences, four boundary conditions and four supplementary equations. ($4(N-2) + 4 + 4 = 4N$). The final system has the form

$$\begin{bmatrix} A_1 & & & & & \\ -I & 2\Delta x P_2 & I & & & \\ & -I & 2\Delta x P_3 & I & & \\ & & \ddots & \ddots & \ddots & \\ & & & -I & 2\Delta x P_{N-1} & I \\ & & & & & A_N \end{bmatrix} \times \begin{bmatrix} S_1 \\ S_2 \\ S_3 \\ \vdots \\ S_{N-1} \\ S_N \end{bmatrix} = \begin{bmatrix} B_1 \\ 2\Delta x Q_2 2 \\ \Delta x Q_3 \\ \vdots \\ 2\Delta x Q_{N-1} \\ B_N \end{bmatrix}$$

where

$$A_1 = \begin{bmatrix} -1 & -\Delta x & 0 & 0 & 1 & 0 & 0 & 0 \\ 0 & -1 & 0 & 0 & 0 & 1 & 0 & 0 \\ 0 & 0 & 1 & 0 & 0 & 0 & 0 & 0 \\ 0 & -F(0) & 0 & 1 & 0 & 0 & 0 & 0 \end{bmatrix}$$

$$A_N = \begin{bmatrix} 0 & 0 & 0 & 0 & 1 & 0 & 0 & 0 \\ 0 & 0 & 0 & 0 & 0 & 1 & 0 & 0 \\ 0 & -1 & 0 & 0 & 0 & 0 & \Delta x D(L)^{-1} & 0 \\ 0 & 0 & -1 & 0 & 0 & 0 & 1 & -\Delta x \end{bmatrix}$$

and

$$B_1 = (0, -\Delta x D(0)^{-1}M_{\mathrm{o}}, M_{\mathrm{o}}, V_{\mathrm{o}})^t, \quad B_N = (0, 0, 0, 0)^t.$$

Once the system is solved, an approximation of the flexure w and the bending moment M is obtained at each point x_n of the interval $[0, L]$ from the first and third components of S_n, $n = 1, \ldots, N$.